SCS 2026

Twenty-second International Scientific Conference

SPACE, ECOLOGY, SAFETY

20 – 24 October 2026, Stara Zagora, Bulgaria

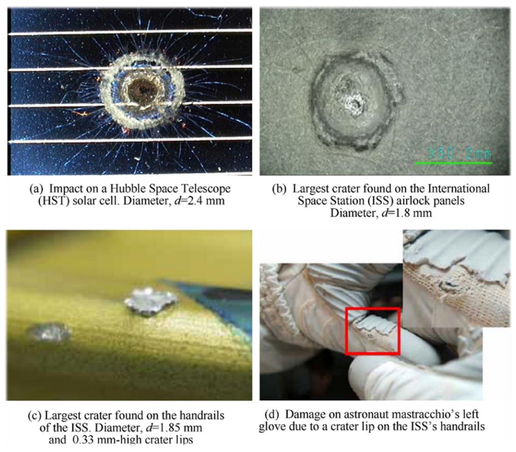
LUNAR EXOGENIC PROCESSES POSING HAZARDS TO LONG-TERM LUNAR INFRASTRUCTURE

Iskren Ivanov, Lachezar Filchev

Space Research and Technology Institute – Bulgarian Academy of Sciences (SRTI-BAS)

Abstract

Humanity's transition from short-duration lunar sorties to the establishment of a continuous human presence on the lunar surface —in the context of NASA's Artemis program, the International Lunar Research Station (ILRS), and ESA's Argonaut lunar lander program—requires ensuring long-term operational reliability within the harsh lunar environment. This review paper consolidates into a unified framework the numerous exogenous hazards identified to date by the aerospace community. It analyzes ongoing impact cratering processes, their morphological features and mechanisms, cosmic ray flux, electrostatic regolith mobilization, and drastic diurnal temperature swings. Ultimately, this review details the specific risks and structural impacts that these phenomena pose to lunar infrastructure and instrumentation.



(a) Impact on a Hubble Space Telescope (HST) solar cell. Diameter, d=2.4 mm

(b) Largest crater found on the International Space Station (ISS) airlock panels Diameter, d=1.8 mm

(c) Largest crater found on the handrails of the ISS. Diameter, d=1.85 mm and 0.33 mm-high crater lips

(d) Damage on astronaut mastracchio's left glove due to a crater lip on the ISS's handrails

Figure 1. Examples of microscale hypervelocity kinetic damage on engineered aerospace components. Micro-crater pitting and glass spallation halos on a solar panel degrade power efficiency. A hypervelocity impact crater on an ISS metallic handrail showcases a sharp rim; tactile contact with these razor-sharp edges causes severe fabric abrasion and tearing of protective EVA spacesuit gloves and dynamic seals, threatening catastrophic pressure loss. The micrometeoroid influx of ~1.4 metric tons/day poses an acute risk that threatens the mechanical integrity of long-term lunar habitats and structural alloys. Sourced from the public author preprint repository of Meyer et al. (2022). Image unmodified [1]

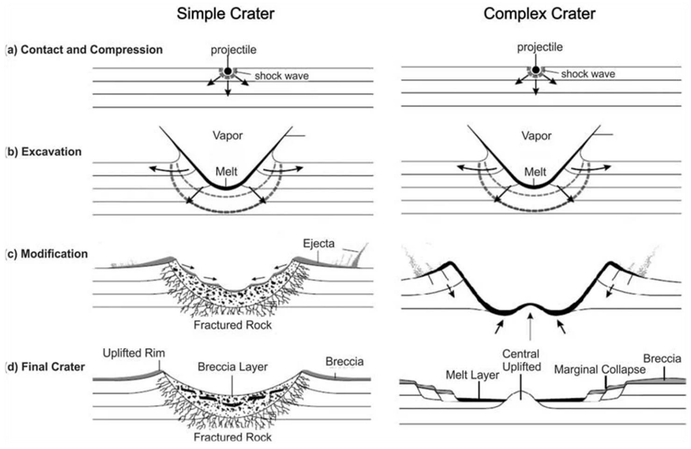


Figure 2. Simple and complex craters stages of formation. Both crater types progress through three fundamental geophysical phases: (1) Contact and Compression, where the projectile transfers hypervelocity kinetic energy into intense subsurface shockwaves; (2) Excavation, where shockwaves displace target material outward to construct a temporary, unstable transient cavity; and (3) Modification, where the final structural morphology diverges by scale: smaller simple craters settle via localized wall failure into a bowl-shaped depression with an unstratified breccia lens, whereas massive complex craters undergo dramatic hydrodynamic rebound, causing the floor to snap violently upward into a permanent central peak ring flanked by highly unstable, terraced walls. Sourced from the public author preprint repository of Ferreira et al. (2015). Image unmodified [2].

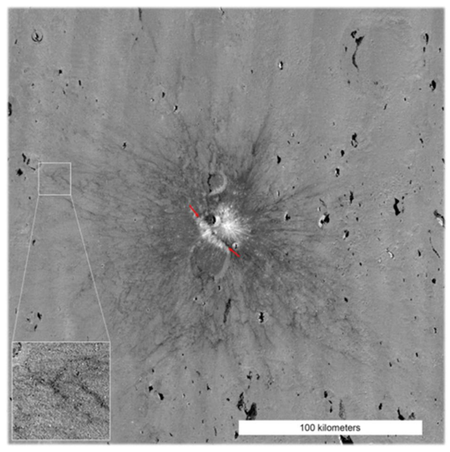


Figure 3. Regional LROC WAC mosaic illustrating an impact site at its center, with north oriented upward. Visible features include a proximal ejecta blanket extending ~15 km outward and a broader, low-reflectance distal zone reaching radial distances of 100 km. The extensive 100-km distal zone poses severe dust contamination hazards; fine, electrostatically charged particles within this low-reflectance terrain can easily coat optical instruments, foul photovoltaic arrays, and occlude thermal radiators. Reprinted from Robinson et al. (2026), under the terms of the Creative Commons Attribution 4.0 International (CC BY 4.0) License [3].

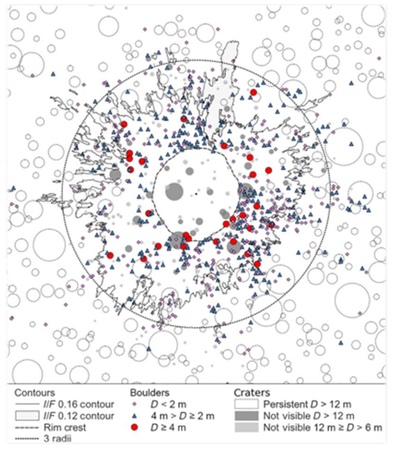


Figure 4. Map delineating the distribution of the ejecta blanket, demonstrating the complete obscuration of the antecedent topography adjacent to the newly formed crater structure (950 m wide, oriented north-up). From an infrastructure standpoint, the ejecta blanket represents a high-risk zone of heavy kinetic loading, material displacement, and total structural burial. Reprinted from Robinson et al. (2026), under the terms of the Creative Commons Attribution 4.0 International (CC BY 4.0) License [3].

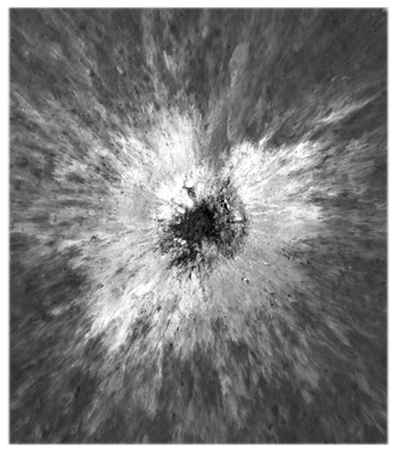


Figure 5. Lunar Reconnaissance Orbiter Camera (LROC) NAC image capturing the newly formed, 222-meter-diameter impact crater (McGetchin crater), resampled at a 1-meter spatial resolution. The feature resulted from a bolide impact that occurred between April 11 and May 22, 2024. Reprinted from Robinson et al. (2026), under the terms of the Creative Commons Attribution 4.0 International (CC BY 4.0) License [3].

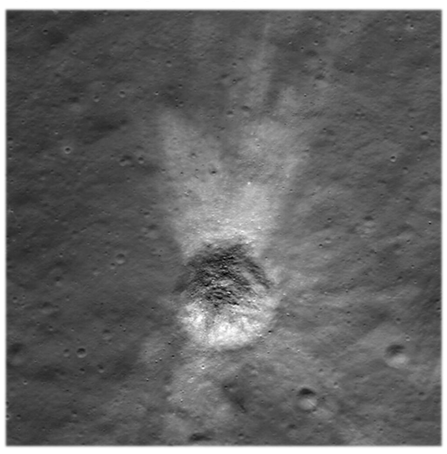


Figure 6. Image of "butterfly-wing" ejecta curtain, producing highly focused, distinct ejecta streams concentrated along specific radial directions. This distinct morphological pattern presents an aggressive directional hazard to surface operations as the focused hypervelocity streams concentrate the kinetic loading of primary fragments and scoured regolith along narrow downrange vectors. Image credit: Lunar Reconnaissance Orbiter Camera (LROC), Arizona State University (ASU) [4].

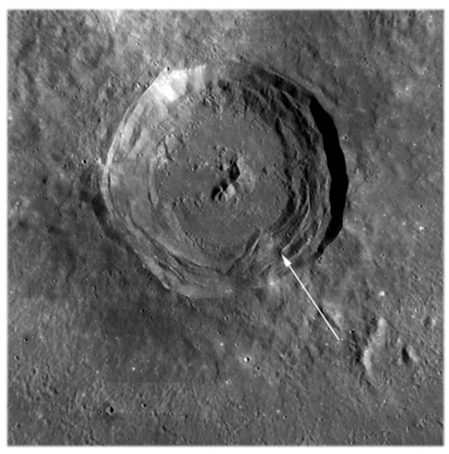


Figure 7. Maunder crater, featuring its distinctive wall terraces formed by lunar mass-wasting events. Subsequent impact events or localized surface operations can readily remobilize this loose, unstratified debris, exacerbating slope instability and triggering downslope mass-wasting or active landslides. Image courtesy of NASA/GSFC/Arizona State University, distributed publicly via the Lunar Reconnaissance Orbiter Camera (LROC) archive [5].

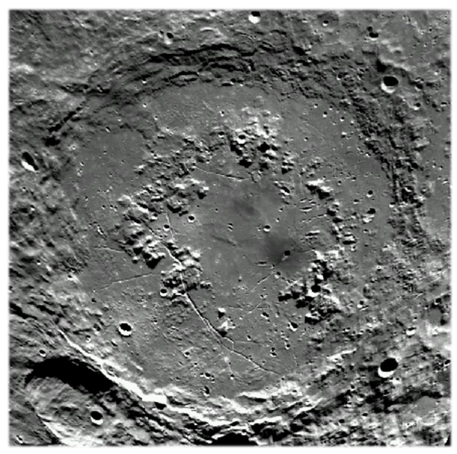


Figure 8. Schrödinger impact basin features a prominent, concentric inner ring of rugged mountains up to 2 km high and consist of deeply uplifted crystalline bedrock. A wide topographic gap breaks the ring structure along its southern margin. The rugged 2-km-high peak-ring massifs and steep outer terraces present risks of localized landslides and persistent structural shadows. The shocked, porous bedrock provides unpredictable load-bearing foundations while the towering topography obstructs critical line-of-sight radio communications. Image credit NASA [6].

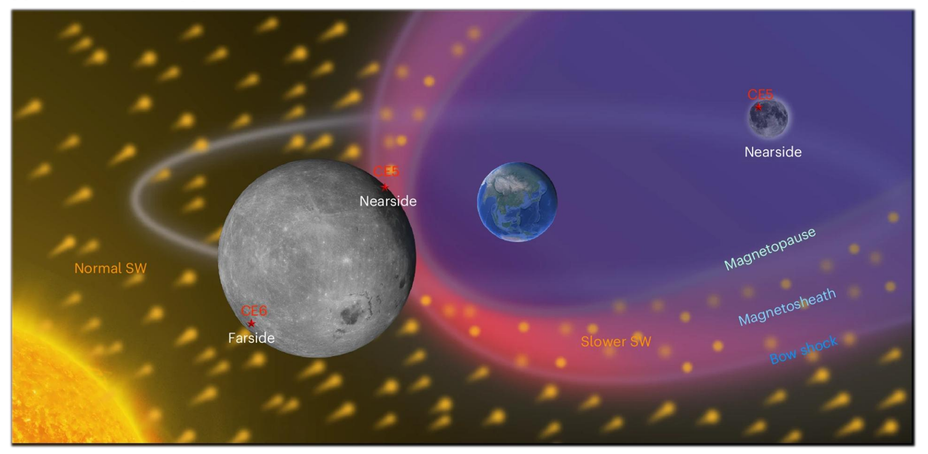


Figure 9. Schematic of solar wind shielding dynamics by Earth's magnetosphere during lunar orbit, highlighting radiation and charging hazards. The purple region represents Earth's magnetosphere, which attenuates and deflects the incoming solar wind. As the Moon traverses the magnetosheath twice per orbit, the Earth-facing near side receives heavily decelerated solar wind (slowing from ~400 km s^{-1} to ~200 km s^{-1}), whereas the tidally locked far side remains entirely unshielded from full-velocity space plasma. This unattenuated particle flux drives severe dielectric charging and Total Ionizing Dose (TID) degradation within surface electronics. At the twilight terminator boundaries, sharp spatial potential gradients exceeding 40 V m^{-1} generate intense horizontal electric fields that trigger microsecond-scale Electrostatic Discharges (ESD). The resulting high-amplitude Electromagnetic Interference (EMI) can penetrate hardware enclosures through shielding seams, inducing critical component latch-up or permanent gate breakdown in unshielded infrastructure.. Reprinted from Zhang et al. (2026), under the terms of the Creative Commons Attribution 4.0 International (CC BY 4.0) License [7].

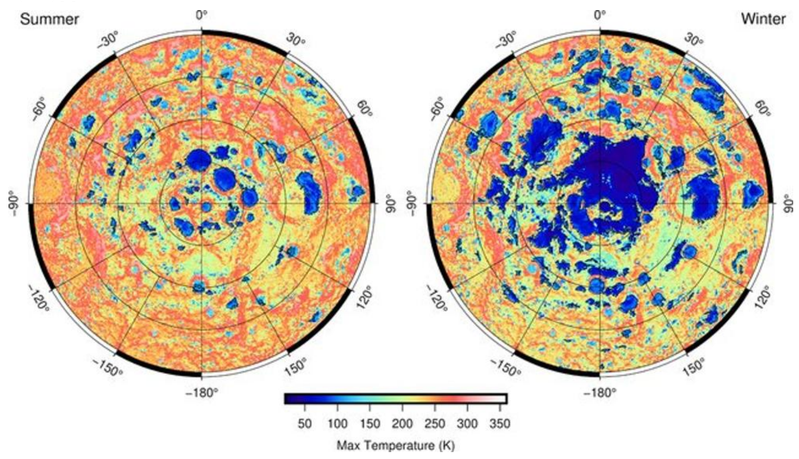


Figure 10. Summer and winter lunar surface temperatures poleward of 80°S latitude derived from Diviner Lunar Radiometer measurements. The thermal maps delineate the permanently shadowed regions (PSRs), which function as cold traps capable of harboring cryogenic volatile ice deposits (lunar water ice). Characterized as some of the coldest ambient environments directly measured within the Solar System. Sourced from the public author preprint repository of Schörghofer et al. (2021). Image unmodified [8].

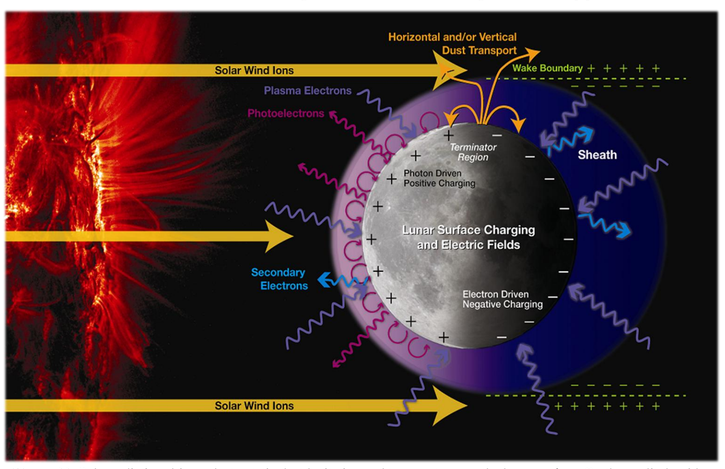
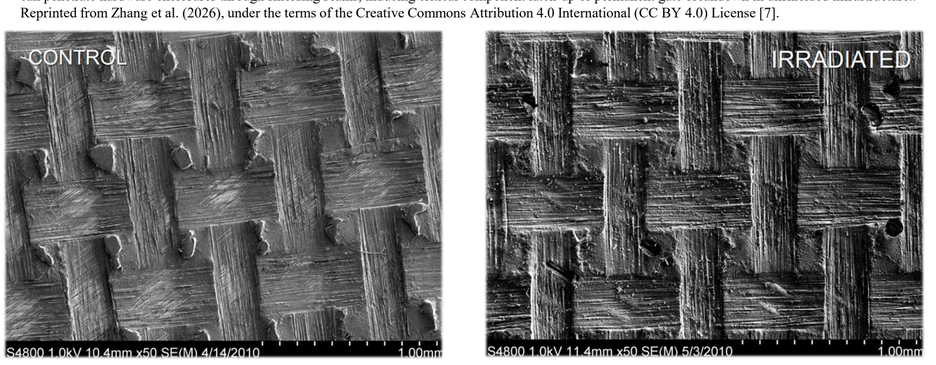


Figure 11. Solar radiation-driven electrostatic dust levitation and transport across the lunar surface. On the sunlit dayside, solar radiation induces photoelectron emission, leaving the dust with a positive electrostatic charge that binds it to the surface. On the nightside, ambient plasma interactions charge the regolith negatively, creating a steep electrical potential gradient at the terminator boundary. The resulting intense horizontal electric fields levitate and mobilize dust particles across the terminator zone, driving a net transport and deposition of regolith from shadowed regions into sunlit terrain. Reproduced from Halekas (n.d.), Royal Belgian Institute for Space Aeronomy public educational database [9].



Figures 12 and 13. Surface morphology and analytical characterization of boron/carbon epoxy composite following simulated long-term lunar environment exposure (30-year). Scanning electron microscopy (SEM) of irradiated matrix surface reveals distinct microstructural degradation resembling localized corrosion, contrasting with the uniform surface profile of the non-irradiated control group. Corresponding Fourier Transform Infrared Spectroscopy (FTIR) difference spectrum analysis indicates a marked destruction of the foundational aromatic network structure alongside increases in the hydroxyl band, C-H stretching, and linear double-bonded configurations, confirming pronounced oxidative degradation. Mechanically, simultaneous exposure to proton radiation and longitudinal/hoop structural tension induced a substantial increase in strength-to-failure and strain-to-failure limits, signaling radiation-enhanced matrix cross-linking. The simulated lunar proton exposure alters the baseline physical and chemical properties of advanced polymer matrices. Reprinted from Rojdev et al. (2010), in the public domain [10].

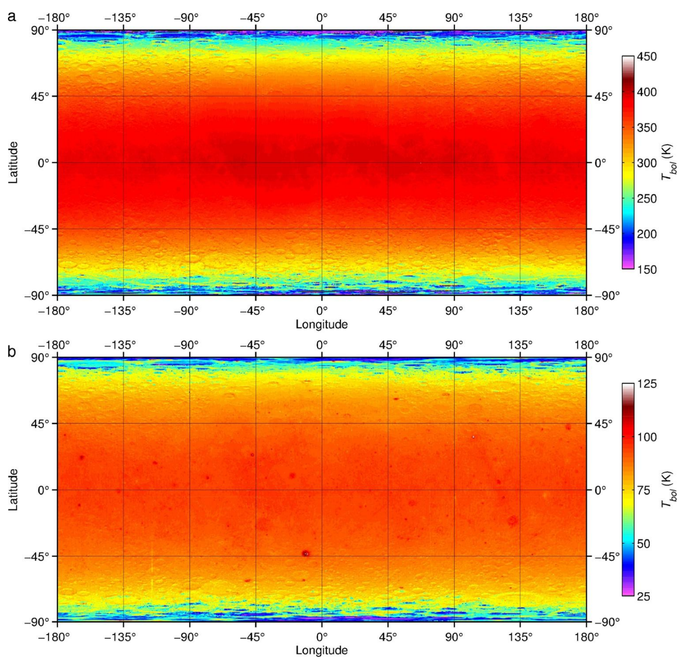


Figure 14. (a) Maximum and (b) minimum global temperatures. Thermal dynamics and environmental hazards governing the longevity of lunar infrastructure. Extreme, high-amplitude cyclic temperature shifts (~95 K to ~397 K) drive severe volumetric expansion and contraction, inducing structural fatigue, weld degradation, and mechanical failures over extended deployment lifetimes. During the 14-Earth-day lunar night, prolonged darkness threatens subsystems with critical failures, including the glass transition of mechanical seals, lubricant degradation, and irreversible battery capacity loss. Reprinted from Williams et al. (2017), under the terms of the Creative Commons Attribution 4.0 International (CC BY 4.0) License [11].

Conclusion

- The lunar surface is a highly volatile, interconnected frontier impacting structural, thermal, and microelectronic systems.
- Next-generation infrastructure (Artemis, ILRS, and Argonaut) will be severely tested by a harsh cross-section of external stressors.
- Systems must survive continuous hypervelocity impacts, extreme thermal gradients (down to 50 K), ionizing radiation, and dynamic dust mobilization.
- Engineering solutions built for these degradation mechanisms form the foundational stepping stone for humanity's expansion to Mars.

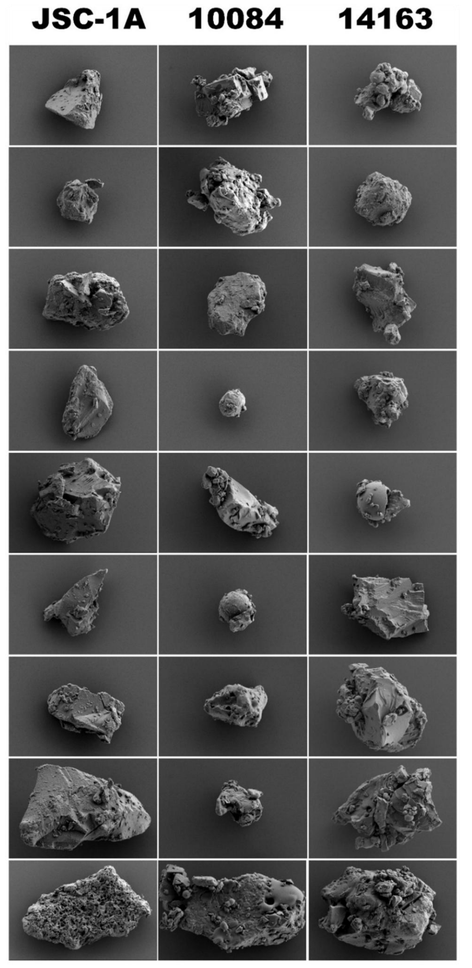


Figure 15. Representative Scanning Electron Microscope (SEM) images of JSC-1A simulant, Apollo 11 (10084), and Apollo 14 (14163) regolith (12.71 µm field width). Micrographs reveal the highly jagged, glass-rich, and razor-sharp morphologies characteristic of native lunar regolith shaped by billions of years of hypervelocity impacts. Without atmospheric weathering to smooth these fragments, unattenuated bombardment yields pristine, comminuted particles. Impact cratering, mass wasting high-velocity lander exhaust plumes and rover wheels forcefully displace these abrasive fragments, while terminator electric fields drive natural electrostatic dust levitation. Once redistributed across nearby infrastructure, the dust reduces solar panels power conversion efficiency, accumulates on dynamic interfaces, accelerating friction and degrading critical mechanical seals. Due to the regolith's low albedo, dust-covered radiators experience drastically increased solar absorption and severe thermal insulation, blocking critical heat rejection and risking system-wide thermal runaway. Sourced from the public author manuscript of Goguen et al. (2024). Image unmodified [12].

References & Image Credits

[1] Meyer, C.S., I.G. Catugas, J.W. Gillespie Jr, B.Z.G. Haque. "Investigation of normal, lateral, and oblique impact of microscale projectiles into unidirectional glass/epoxy composites." "Defence Technology", 2022, 18(11), 1960–1978

[2] Ferreira, J.C., E.P. Leite, M.A.R. Vasconcelos, A.P. Crósta. "3D gravity modeling of impact structures in basaltic formations in Brazil: Part I–Vargeão, Santa Catarina." "Revista Brasileira de Geofísica", 2015, 33(2), doi:10.22564/rbgf.v33i2.723

[3] Robinson, M.S., A.K. Boyd, P.Mahanti, M.R. Manheim, E.J. Speyerer, J.D. Stopar, R.V. Wagner. "A new 222-m diameter lunar crater." "Science Advances", 2026, 12(38), eaeh7812, doi:10.1126/sciadv.aeh7812

[4] Braden, S. "Asymmetric Ejecta [Image]." "Lunar Reconnaissance Orbiter Camera", 2009, lroc.im-ldi.com, last visited 25.09.2026

[5] Enns, D. "Maunder's Terrace [Image]." "Lunar Reconnaissance Orbiter Camera", 2011, lroc.im-ldi.com, last visited 25.09.2026

[6] NASA. "Schrödinger crater [Image]." "ESA Multimedia", 2019, https://www.esa.int/ESA_Multimedia/Images/2019/07/Schroedinger_crater, last visited 25.09.2026

[7] Zhang, X.H., F. Su, Y.J. Li, Z.H. Liu, J.N. Li, Y.N. Zhang, L.P. Qin, R.R. Liu, F. Man, B. Xu, W.Z. Li, Y. Wei, H.Y. He. "Deeper solar wind penetration on the Moon's farside from noble gas records." "Nature Geoscience", 2026, 19, 887–892, doi:10.1038/s41561-026-02042-w

[8] Schörghofer, N., M. Benna, A.A. Berezhnoy, B. Greenhagen, B.M. Jones, S. Li, C. Wöhler. "Water group exospheres and surface interactions on the Moon, Mercury, and Ceres." "Space Science Reviews", 2021, 217(6), 74, doi:10.1007/s11214-021-00846-3

[9] Halekas, J. "Charging mechanism of lunar dust [Infographic]." "Royal Belgian Institute for Space Aeronomy", n.d., https://www.aeronomie.be/en/encyclopedia/electrostatic-force-dust-moon, last visited 25.09.2026

[10] Rojdev, K., M.J. O'Rourke, S. Koontz, J. Alred, C. Hill, R. Devivar, S. Morera-Felix, W. Atwell, S. Nutt, L. Sabban, J. Franklin. "Long-term lunar radiation degradation effects on materials." "National Space and Missile Materials Symposium 2010", 2010

[11] Williams, J.P., D.A. Paige, B.T. Greenhagen, E. Sefton-Nash. "The global surface temperatures of the Moon as measured by the Diviner Lunar Radiometer Experiment." "Icarus", 2017, 283, 300–325, doi:10.1016/j.icarus.2016.08.012

[11] Goguen, J., A. Sharits, A. Chiaramonti, T. Lafarge, E. Garboczi. "Three-dimensional characterization of particle size, shape, and internal porosity for Apollo 11 and Apollo 14 lunar regolith and JSC-1A lunar regolith soil simulant." "Icarus", 2024, 420, 116166, doi:10.1016/j.icarus.2024.116166



Ch. Asst. Prof. Dr. Iskren Ivanov
Department of Remote Sensing and GIS
Space Research and Technology Institute
Bulgarian Academy of Sciences
iso.ivanov@space.bas.bg





Professor Dr. Lachezar Filchev
Department of Remote Sensing and GIS
Space Research and Technology Institute
Bulgarian Academy of Sciences
lachezarhf@space.bas.bg